

# Insights in Utilizing $\text{NiCo}_2\text{O}_4/\text{Co}_3\text{O}_4$ Nanowires as Anode Material in Lithium-Ion Batteries

Anubha Tomar<sup>+</sup><sup>[a]</sup>, Egy Adhitama<sup>+</sup><sup>\*[b, c]</sup>, Martin Winter,<sup>[b, d]</sup> Tobias Placke,<sup>[b]</sup> and Alok Kumar Rai<sup>\*[a]</sup>

In this study, a facile and cost-effective hydrothermal approach is employed to synthesize a mesoporous  $\text{NiCo}_2\text{O}_4/\text{Co}_3\text{O}_4$  nanocomposite with nanowire morphology by using polyvinyl pyrrolidone as structure-directing agent. The obtained  $\text{NiCo}_2\text{O}_4/\text{Co}_3\text{O}_4$  nanocomposite shows better electrochemical performance than pure  $\text{NiCo}_2\text{O}_4$  due to mainly two reasons: i) a strong synergistic effect between  $\text{NiCo}_2\text{O}_4$  and  $\text{Co}_3\text{O}_4$ , which enhances the  $\text{Li}^+$  diffusion rate as well as lower the charge-transfer resistance, and ii) the involvement of  $\text{Co}_3\text{O}_4$  to contribute to the total capacity due to its high electrochemical activity. However, the performance of a  $\text{NiCo}_2\text{O}_4/\text{Co}_3\text{O}_4$  nanocomposite electrode

starts degrading after 400 cycles while pure  $\text{NiCo}_2\text{O}_4$  maintains steady performance. Since the  $\text{NiCo}_2\text{O}_4/\text{Co}_3\text{O}_4$  nanocomposite sample shows high porosity, it is believed that the obtained nanowire morphology cannot tolerate volume variations, which are generally triggered off during repeated  $\text{Li}^+$  (de-)insertion at long-term cycling. Therefore, the obtained results bring new insights in terms that there is a sweet spot between  $\text{Li}^+$  diffusion and high porosity in utilizing  $\text{Co}_3\text{O}_4$  within a nanocomposite. This study is of guidance to shed the light on the research of ternary transition metal oxide nanocomposite materials for lithium-ion batteries.

## Introduction

With the advent of new technologies, our daily life has become advanced and moving forward at a high speed and thus enormous growth has been registered in every sector of the market. However, this rapid growth has given momentum to the biggest crisis of this era, i.e., climate and energy. The continuous depletion of non-renewable sources and the limited supply of energy from renewable sources at high cost expedited the investigation for numerous alternatives to meet the present energy demands for a longer duration.<sup>[1]</sup> Among all the investigations, lithium-ion batteries (LIBs) have already achieved great success as energy storage devices for many applications.<sup>[2]</sup> However, the use of LIBs for advanced applications such as for electric vehicles is limited due to their energy density, safety performance, and cost.<sup>[3–6]</sup> Recently, transition

metal oxides, using metals such as Fe, Mn, Ni, Co, Cr, etc., have been actively proposed as a replacement for the graphite anode due to the various advantages for example their high theoretical specific capacity ( $> 500 \text{ mAh g}^{-1}$ ), excellent electrochemical properties, diverse morphological characteristics, and reversible redox reaction, high abundance, low cost, and environmental friendliness.<sup>[7–13]</sup> Furthermore, the research interest in this field continued with ternary transition metal oxides due to their distinctive chemical component, abundant active sites, synergistic combination of various metals, and high redox activity.<sup>[14–16]</sup> In addition, a partial replacement of binary oxides by suitable transition metal ions opens the class of ternary oxides. In regard to the ternary oxide of  $\text{NiCo}_2\text{O}_4$ , the synergistic effect of two different metal ions (i.e.,  $\text{Ni}^{2+}$  and  $\text{Co}^{3+}$ ) lowers the band gap and activation energy for electron transfer, resulting in the improved redox reactions and higher electronic conductivity compared to binary oxides of  $\text{Co}_3\text{O}_4$  and  $\text{NiO}$ .<sup>[17, 18]</sup>

Despite the fact that these metal oxides will have no application in LIBs due to the high costs of Co and Ni and their environmental concerns, the motivation of this work comes from the interest in new materials and their synthesis processes followed by performances along with the understanding of the redox mechanisms. In addition, though  $\text{NiCo}_2\text{O}_4$  has a high theoretical capacity of approximately  $\sim 891 \text{ mAh g}^{-1}$ , it also suffers from poor electronic conductivity, sluggish  $\text{Li}^+$  diffusion kinetics, and electrode pulverization induced by huge volume changes during the lithiation and delithiation processes, resulting in fast capacity fading and poor rate capability.<sup>[19]</sup> To address all these challenges of  $\text{NiCo}_2\text{O}_4$ , numerous strategies have been proposed such as the synthesis of nanostructures with high porosity, fabrication of nanocomposites with carbonaceous compounds, novel and sustainable morphology with less structural strain to achieve high surface area for fast

[a] A. Tomar,<sup>+</sup> Dr. A. K. Rai  
Department of Chemistry  
University of Delhi  
Delhi-110007 (India)  
E-mail: alokkumarrai1@gmail.com

[b] E. Adhitama,<sup>+</sup> Prof. M. Winter, Dr. T. Placke  
MEET Battery Research Center, Institute of Physical Chemistry  
University of Münster  
Corrensstr. 46, 48149 Münster (Germany)  
E-mail: egyadhitama@uni-muenster.de

[c] E. Adhitama<sup>\*</sup>  
International Graduate School for Battery Chemistry, Characterization, Analysis, Recycling and Application (BACCARA)  
University of Münster  
Corrensstr. 40, 48149 Münster (Germany)

[d] Prof. M. Winter  
Helmholtz Institute Münster  
IEK-12, Forschungszentrum Jülich GmbH  
Corrensstr. 46, 48149 Münster (Germany)

[+] These authors contributed equally to this paper.

diffusion of  $\text{Li}^+$  ions.<sup>[14,20]</sup> However, one of the key approaches to fabricate a nanocomposite of  $\text{NiCo}_2\text{O}_4$  with other binary transition metal oxides, such as  $\text{NiCo}_2\text{O}_4/\text{Fe}_2\text{O}_3$ ,<sup>[21]</sup>  $\text{NiCo}_2\text{O}_4/\text{NiO}$ ,<sup>[22]</sup>  $\text{NiCo}_2\text{O}_4/\text{TiO}_2$ ,<sup>[23]</sup>  $\text{NiCo}_2\text{O}_4/\text{MnO}_2$ ,<sup>[24]</sup> was found promising due to the strong synergistic effect between two different metal ions, volume variation in sequences due to two different working voltages, high mechanical stability, and high electronic/ionic conductivity.<sup>[25]</sup> Therefore, the objective of the present work is to prepare a nanocomposite of  $\text{NiCo}_2\text{O}_4/\text{Co}_3\text{O}_4$  using the nonstoichiometric ratio of Ni and Co. It is always unique if an extra amount of binary transition metal oxide is generated from the host material with distinctive nanostructures using cost-effective synthesis methods.

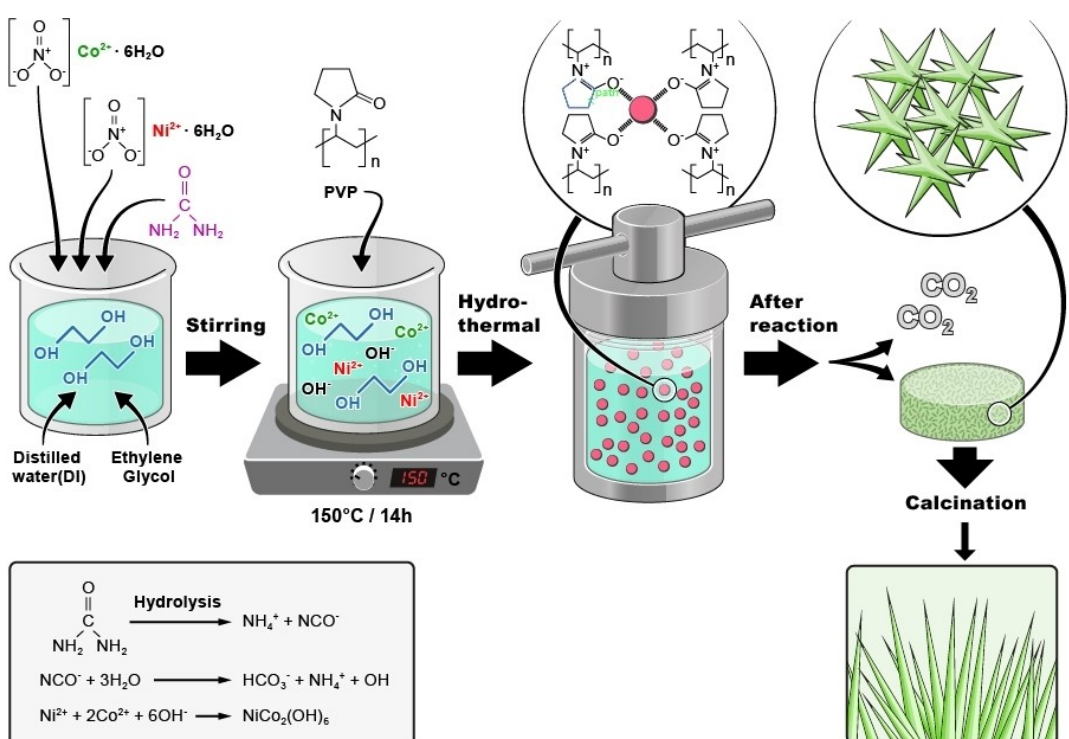
The present work demonstrates the synthesis of one-dimensional (1D)  $\text{NiCo}_2\text{O}_4/\text{Co}_3\text{O}_4$  nanocomposite with nanowire morphology by adjusting the molar ratio of Ni and Co precursors via a facile low-cost hydrothermal approach. In this strategy, poly(vinylpyrrolidone) (PVP) served as a structure-directing agent to lead the anisotropic growth of porous material through the coordination of functional groups of  $-\text{N}$  and  $=\text{C}=\text{O}$  of the pyrrolidone ring with metal ions. On the other hand,  $\text{NH}_4^+$  and  $\text{OH}^-$  produced as a result of the decomposition of urea offer a basic medium to synthesize metal-hydroxide crystals via the nucleation process. Furthermore, pure  $\text{NiCo}_2\text{O}_4$  was also prepared using the stoichiometric ratio to compare the electrochemical performances with the  $\text{NiCo}_2\text{O}_4/\text{Co}_3\text{O}_4$  nanocomposite. The obtained  $\text{NiCo}_2\text{O}_4/\text{Co}_3\text{O}_4$  nanocomposite exhibits superior electrochemical performances in terms of capacity, rate performances, and cycling stability than pure  $\text{NiCo}_2\text{O}_4$ . It is believed that the excellent perform-

ances of the nanocomposite may be due to the existence of an extra phase of  $\text{Co}_3\text{O}_4$  (tuning of redox couple of  $\text{Co}^{2+}/\text{Co}^{3+}$ ) along with porosity, which buffers the volume expansion/contraction during cycling and improves the structural stability. It is essential to point out that the phenomena discussed in this study can further navigate the direction of research to improve  $\text{NiCo}_2\text{O}_4$  performances.

## Results and Discussions

### Crystal structure and morphological studies

Scheme 1 exhibits the synthesis procedure used in this work for the fabrication of 1D nanowires of pure  $\text{NiCo}_2\text{O}_4$  and  $\text{NiCo}_2\text{O}_4/\text{Co}_3\text{O}_4$  nanocomposite samples. Figure 1(a) shows the TG/DTA curves of the as-prepared pure  $\text{NiCo}_2\text{O}_4$  sample, which clearly shows a weight loss of nearly  $\sim 27\%$  between  $200^\circ\text{C}$  to  $350^\circ\text{C}$  due to the degradation of organic moieties. The exothermic DTA curve is in the accordance with TGA results. Since there is no significant weight loss observed above  $400^\circ\text{C}$ , the calcination of as-prepared samples was performed at  $400^\circ\text{C}$ , which is remarkably low in comparison to other reported data.<sup>[13,23]</sup> To determine the phase purity and crystallinity of the calcined samples, XRD analysis was performed. As can be seen from Figure 1(b), all the reflections of pure  $\text{NiCo}_2\text{O}_4$  sample can be ideally indexed with the standard JCPDS data (No. 02-0781) of cubic  $\text{NiCo}_2\text{O}_4$  without any other impurity. More importantly, the XRD reflections of the nanocomposite sample also perfectly match with the JCPDS data of cubic



Scheme 1. Schematic illustration of the synthesis of 1D nanowire samples.

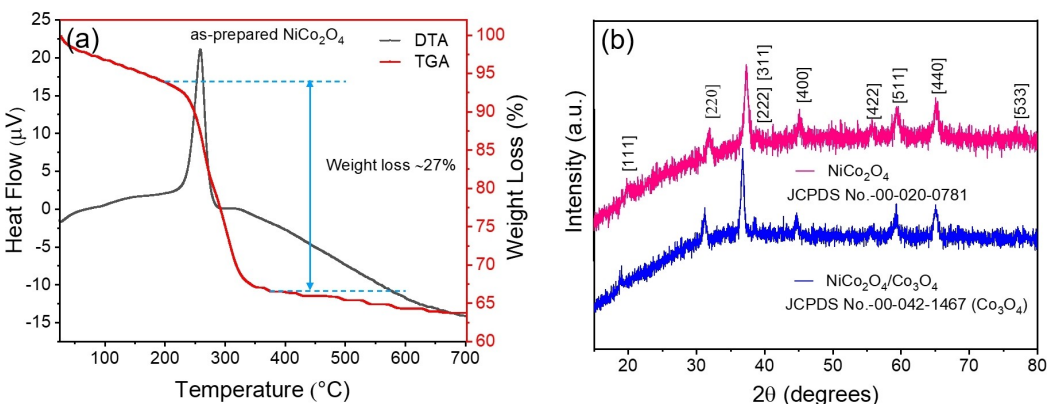


Figure 1. a) TG/DTA of the as-prepared sample; b) XRD patterns of calcined pure  $\text{NiCo}_2\text{O}_4$  and  $\text{NiCo}_2\text{O}_4/\text{Co}_3\text{O}_4$  nanocomposite samples, respectively.

**Table 1.** Chemical composition and phase fraction analysis of pure  $\text{NiCo}_2\text{O}_4$  and  $\text{NiCo}_2\text{O}_4/\text{Co}_3\text{O}_4$  nanocomposite.

Target composition	ICP concentration [wt %]	Practical mole composition (Normalized to Co)
$\text{NiCo}_2\text{O}_4$	Ni Co 20.62 37.51	$\text{Ni}_{1.103}\text{Co}_2\text{O}_4$
Phase fraction calculation of $\text{NiCo}_2\text{O}_4$ and $\text{Co}_3\text{O}_4$		
Target composition	ICP calculation Phase calculation	
Element	ICP value [wt %]	Practical molar ratio (Normalized to Ni as 1)
$\text{NiCo}_2\text{O}_4/\text{Co}_3\text{O}_4$	Ni Co	1 2.52
	15.33 38.72	— 0.52
		Composition $\text{NiCo}_2\text{O}_4$ $\text{Co}_3\text{O}_4$
		Phase fraction 0.79 0.21

$\text{NiCo}_2\text{O}_4$  and cubic  $\text{Co}_3\text{O}_4$  (JCPDS file no. 042–1467). Since the 2-theta value of all the reflections of  $\text{NiCo}_2\text{O}_4$  and  $\text{Co}_3\text{O}_4$  are exactly the same, it is rather difficult to differentiate them.

In order to know the exact ratio of Ni and Co in the designed  $\text{NiCo}_2\text{O}_4/\text{Co}_3\text{O}_4$  nanocomposite and pure  $\text{NiCo}_2\text{O}_4$  samples, an ICP-AES study was also carried out and the results are shown in Table 1. It can be noticed that the chemical composition of the pure  $\text{NiCo}_2\text{O}_4$  is close to the stoichiometric ratio as targeted. In contrast, the phase fraction ratio between  $\text{NiCo}_2\text{O}_4$  and  $\text{Co}_3\text{O}_4$  in the nanocomposite sample is found to be nearly ~0.72 and ~0.21, respectively, which clearly confirmed that the nanocomposite sample has an extra phase of cobalt oxide as per our planned strategy.

The structural and morphological features of both pure  $\text{NiCo}_2\text{O}_4$  and  $\text{NiCo}_2\text{O}_4/\text{Co}_3\text{O}_4$  nanocomposite samples were analyzed using FE-SEM, FE-TEM, and selected area electron diffraction (SAED) analysis. The FE-SEM images of both the samples taken at different regions and magnifications clearly show the nanowire-like morphology with porous structure, as illustrated in Figure 2(a, b) and (c, d), respectively. However, it can be easily noticed from Figure 2(d) that the nanocomposite sample has a higher porosity than the pure  $\text{NiCo}_2\text{O}_4$  sample. On the other hand, it also seems that the nanocomposite nanowires are uniformly aligned in comparison to pure  $\text{NiCo}_2\text{O}_4$  sample.

Furthermore, the FE-TEM images of pure  $\text{NiCo}_2\text{O}_4$  and  $\text{NiCo}_2\text{O}_4/\text{Co}_3\text{O}_4$  nanocomposite samples were also recorded and the obtained results are in good correlation to the FE-SEM

results. It can be clearly seen that the nanowire-like morphology is mainly composed by small interconnected primary nanoparticles with a size of ~9–20 nm, as shown in Figure 3(a and d). However, it should be first noticed that the nanoparticles of the nanocomposite sample seem not to be tightly connected as like pure sample-, resulting in the length of the nanowire size (Figure 3d) being smaller than the pure sample (Figure 3a), which also confirmed the high porosity of the nanocomposite sample. It is believed that the nanocomposite nanowires could not hold the structure for a longer time due to high porosity. Furthermore, the HR-TEM images of both samples demonstrate similar lattice fringes with the spacing of approximately ~0.46 and ~0.24 nm, which corresponds to the (111) and (311) planes of  $\text{NiCo}_2\text{O}_4$ , respectively, as shown in Figure 3(b–e). As mentioned above, the  $\text{NiCo}_2\text{O}_4$  and  $\text{Co}_3\text{O}_4$  have similar XRD patterns and thereby the separate lattice fringes are difficult to find for both oxides. The selected area electron diffraction (SAED) patterns of both the samples (Figure 3c and f) exhibit the same diffraction rings for the planes of (220), (311), (400) and (111), which are also in good agreement with the XRD pattern of  $\text{NiCo}_2\text{O}_4$ , confirming the purity of both samples.

To examine the specific surface area and porosity of both the samples, the BET adsorption-desorption and their corresponding pore-size distribution (insets) based on Barrett-Joyner-Halenda (BJH) method has been performed, as shown in Figure 4(a and b). As can be seen that both the samples of pure  $\text{NiCo}_2\text{O}_4$  and  $\text{NiCo}_2\text{O}_4/\text{Co}_3\text{O}_4$  nanocomposite showed a

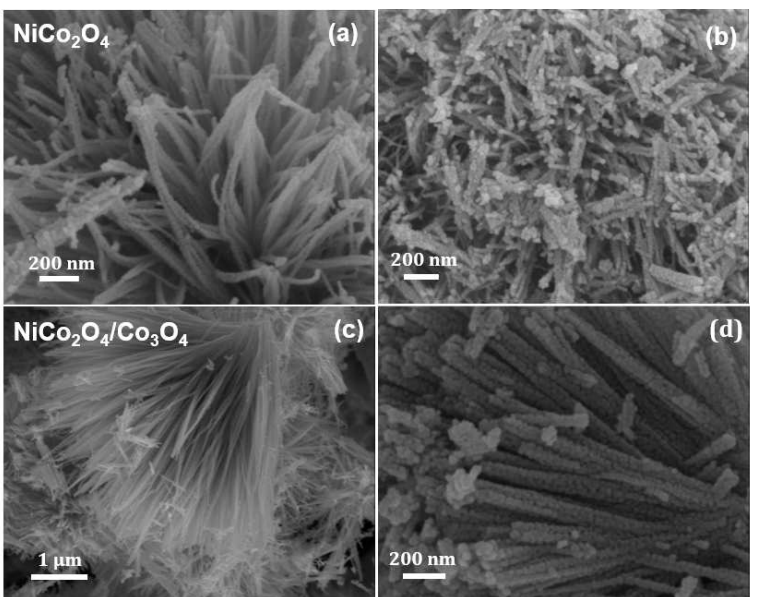


Figure 2. FE-SEM images of a, b) pure  $\text{NiCo}_2\text{O}_4$  and c, d)  $\text{NiCo}_2\text{O}_4/\text{Co}_3\text{O}_4$  nanocomposite samples.

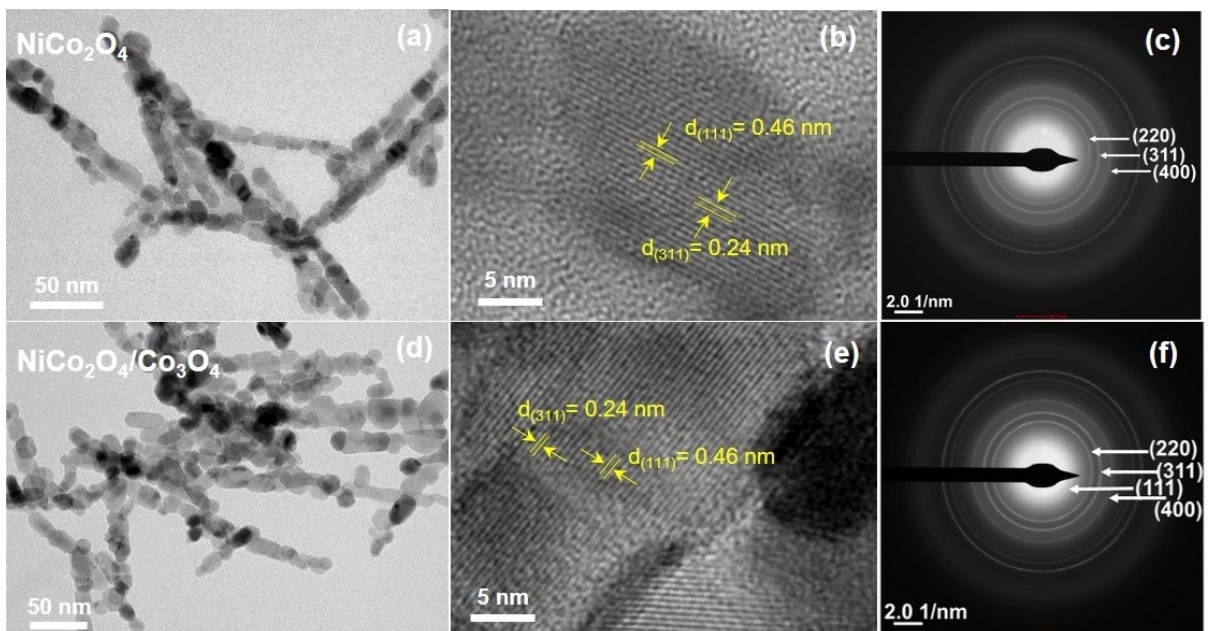


Figure 3. a, d) FE-TEM images; b, e) HR-TEM images and c, f) corresponding SAED patterns of pure  $\text{NiCo}_2\text{O}_4$  and  $\text{NiCo}_2\text{O}_4/\text{Co}_3\text{O}_4$  nanocomposite samples, respectively.

typical type-IV isotherm curve with a hysteresis loop, indicating the mesoporous nature of the samples. The BET surface area is found to be  $\sim 56.2 \text{ m}^2 \text{ g}^{-1}$  and  $\sim 47.1 \text{ m}^2 \text{ g}^{-1}$  for pure and nanocomposite samples, respectively.

However, the pore diameter of  $\text{NiCo}_2\text{O}_4$  and  $\text{NiCo}_2\text{O}_4/\text{Co}_3\text{O}_4$  nanocomposite is nearly in the range of  $\sim 7.5\text{--}15.5 \text{ nm}$  and  $\sim 9\text{--}24 \text{ nm}$ , respectively. The obtained results also showed that the specific surface area of the nanocomposite sample decreases with the introduction of  $\text{Co}_3\text{O}_4$  due to the large pore size between the nanoparticles.

To investigate the surface chemical composition and oxidation states of the ions in  $\text{NiCo}_2\text{O}_4/\text{Co}_3\text{O}_4$  nanocomposite, XPS was carried out and the obtained results are displayed in Figure 5(a-d). As can be seen from Figure 5(a), only Ni, Co, O, and C elements are present in the full survey spectrum of the sample. The C 1s peak of adventitious carbon appeared at  $\sim 284.8 \text{ eV}$  and is used here as a reference for calibration. Furthermore, the Ni 2p, Co 2p, and O 1s spectra are fitted with XPSPEAK 4.1 software under linear-type background. The high-resolution Ni 2p spectrum exhibits spin-orbit doublets which correspond to  $\text{Ni } 2p_{3/2}$  and  $\text{Ni } 2p_{1/2}$  components, as displayed in

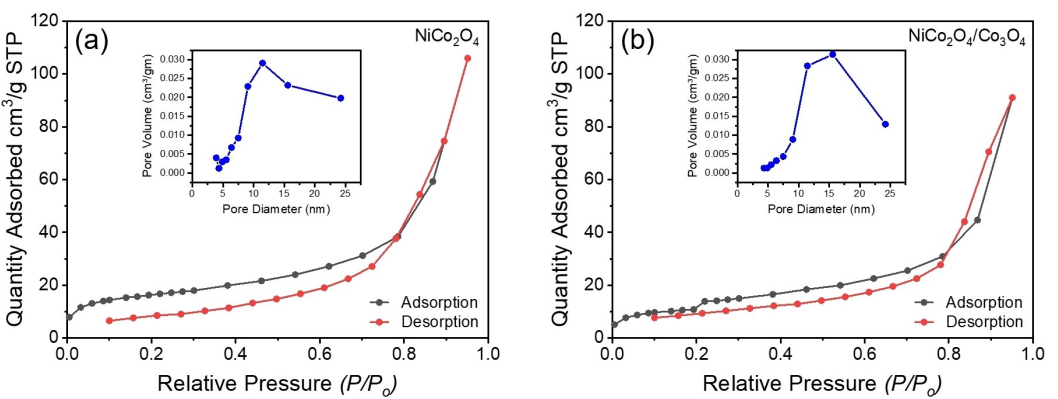


Figure 4. N<sub>2</sub> adsorption/desorption isotherms and pore size distributions (insets) of a) pure NiCo<sub>2</sub>O<sub>4</sub> and b) NiCo<sub>2</sub>O<sub>4</sub>/Co<sub>3</sub>O<sub>4</sub> nanocomposite.

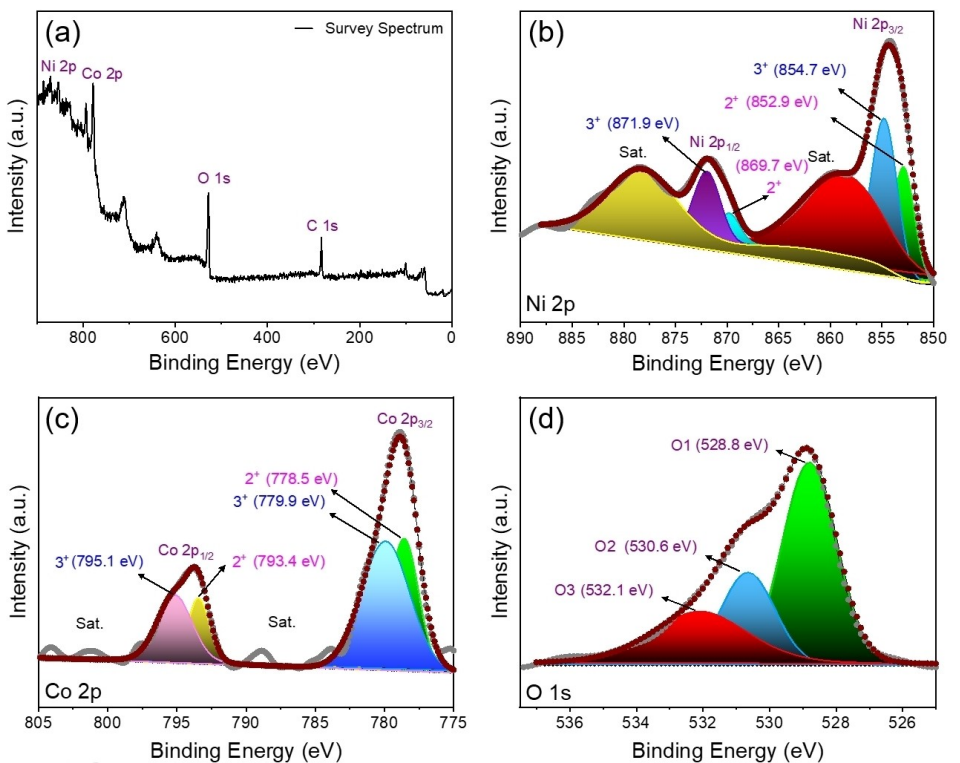


Figure 5. XPS spectra a) survey spectrum; b) Ni 2p; c) Co 2p; d) O1s of NiCo<sub>2</sub>O<sub>4</sub>/Co<sub>3</sub>O<sub>4</sub> sample.

Figure 5(b). Each of these components are deconvoluted to the binding energy of ~854.7 eV and ~871.9 eV and ~852.9 eV and ~869.7 eV, which can be clearly ascribed to the Ni<sup>3+</sup> and Ni<sup>2+</sup> states of Nickel, respectively. Besides the core peaks of Ni 2p, the two shakeup satellites peaks are also observed, which are marked with "Sat." in the figure. Similarly, the high-resolution Co 2p spectrum also consists of the two spin-orbit doublets of Co 2p<sub>3/2</sub> and Co 2p<sub>1/2</sub> with two shakeup satellite peaks, as shown in Figure 5(c). The deconvoluted binding energy peaks obtained at ~779.9 eV and ~795.1 eV belongs to Co<sup>3+</sup>, while the other peaks appeared at ~778.5 eV and ~793.4 eV confirming the Co<sup>2+</sup> state of Cobalt. Furthermore, the high-resolution O 1s spectrum, as represented in Figure 5(d), clearly shows three peaks, which are named as O1, O2 and O3,

respectively. The O1 peak at ~528.8 eV corresponds to the metal-oxygen bond (Ni–O and Co–O), whereas the O2 and O3 peak at ~530.6 eV and ~532.1 eV related to the oxygen vacancies and physically/chemically adsorbed water on the surfaces, respectively. The obtained results confirmed that the chemical composition of the NiCo<sub>2</sub>O<sub>4</sub>/Co<sub>3</sub>O<sub>4</sub> nanocomposite sample contained Ni<sup>3+</sup>, Ni<sup>2+</sup>, Co<sup>3+</sup> and Co<sup>2+</sup>, which are in good agreement with the previous reports.<sup>[11,22]</sup>

### Electrochemical performance studies

To investigate the lithium storage capability of the calcined samples of pure NiCo<sub>2</sub>O<sub>4</sub> and NiCo<sub>2</sub>O<sub>4</sub>/Co<sub>3</sub>O<sub>4</sub> nanocomposite,

cyclic voltammetry (CV) was first performed at a scan rate of  $0.025 \text{ mV s}^{-1}$  within the voltage range of  $0.01\text{--}3.00 \text{ V}$ . Figure 6(a and b) shows the CV curves of the initial five cycles for pure  $\text{NiCo}_2\text{O}_4$  and  $\text{NiCo}_2\text{O}_4/\text{Co}_3\text{O}_4$  nanocomposite cells, respectively. During the first cathodic scan, both the electrodes show a sharp reduction peak at  $\sim 0.8 \text{ V}$  and one minor peak at  $\sim 1.1\text{--}1.2 \text{ V}$  for the nanocomposite electrode, which is due to the reduction of  $\text{Ni}^{2+}$  and  $\text{Co}^{3+}$  to metallic Ni and Co along with the formation of  $\text{Li}_2\text{O}$  [Eq. (1)] and the solid electrolyte interphase (SEI) that resulted from electrolyte decomposition.<sup>[26,27]</sup> In contrast, the two anodic peaks can be also seen for both the electrodes at  $\sim 1.4 \text{ V}$  and  $\sim 2.1 \text{ V}$ , which could be assigned to the oxidation of Ni and Co metals to  $\text{Ni}^{2+}$  and  $\text{Co}^{3+/2+}$ , respectively.<sup>[28,29]</sup> During the second cathodic scan, the reduction peak obtained at  $\sim 0.8 \text{ V}$  shifted to the higher potential of  $\sim 1.1 \text{ V}$ , due to the improved reaction kinetics after

the first lithiation. Conversely, the oxidation peak positions remain the same in the subsequent cycles, indicating the high electrochemical reversibility in the repeated cycles. The lithium storage mechanism for  $\text{NiCo}_2\text{O}_4$  electrode can be clearly illustrated as follows:<sup>[11,30,31]</sup>

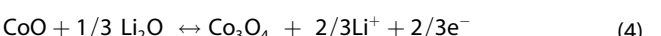
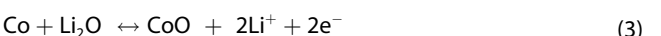
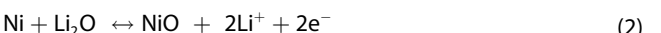
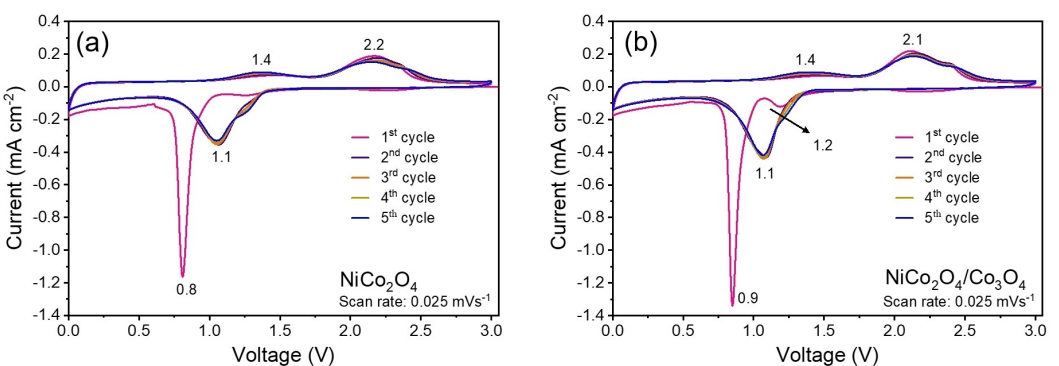
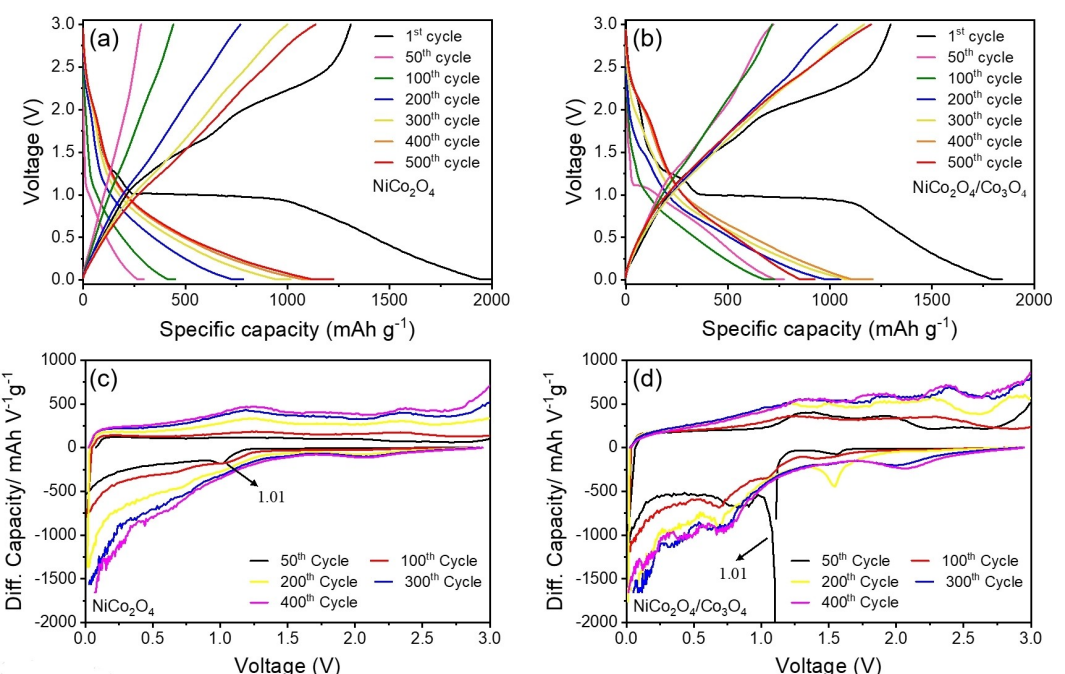


Figure 7(a and b) shows the 1<sup>st</sup>, 50<sup>th</sup>, 100<sup>th</sup>, 200<sup>th</sup>, 300<sup>th</sup>, 400<sup>th</sup>, and 500<sup>th</sup> galvanostatic charge/discharge curves of the



**Figure 6.** Cyclic voltammetry curves of a) pure  $\text{NiCo}_2\text{O}_4$  and b)  $\text{NiCo}_2\text{O}_4/\text{Co}_3\text{O}_4$  nanocomposite electrodes for the initial five cycles at a scan rate of  $0.025 \text{ mV s}^{-1}$  within the voltage range of  $0.01\text{--}3.0 \text{ V}$ .



**Figure 7.** a, b) Galvanostatic charge/discharge curves for the 1<sup>st</sup>, 50<sup>th</sup>, 100<sup>th</sup>, 200<sup>th</sup>, 300<sup>th</sup>, 400<sup>th</sup> and 500<sup>th</sup> cycles at 0.5 C and c, d) the differential capacity vs. voltage curves of pure  $\text{NiCo}_2\text{O}_4$  and  $\text{NiCo}_2\text{O}_4/\text{Co}_3\text{O}_4$  nanocomposite electrodes, respectively.

pure  $\text{NiCo}_2\text{O}_4$  and  $\text{NiCo}_2\text{O}_4/\text{Co}_3\text{O}_4$  nanocomposite electrodes, respectively, at a constant current rate of 0.5 C (1 C = 890  $\text{mA g}^{-1}$ ) between 0.01–3.0 V. The first discharge (=lithiation) curves of both the electrodes displayed short and long-range voltage plateaus at ~1.2 V and ~1.01 V followed by a gradual slope to the cut-off potential of ~0.01 V, which can be ascribed to the reduction of  $\text{Ni}^{2+}$  and  $\text{Co}^{3+}$  to metallic Ni and Co, respectively along with the formation of an SEI.<sup>[13,32]</sup> On the other hand, a broad oxidation peak between ~2.0 V to 2.5 V can be also seen in the charge curve of both electrodes, indicating the oxidation of metallic Ni and Co to  $\text{Ni}^{2+}$  and  $\text{Co}^{3+}/\text{Co}^{2+}$ , respectively. The initial discharge/charge capacity of pure  $\text{NiCo}_2\text{O}_4$  and  $\text{NiCo}_2\text{O}_4/\text{Co}_3\text{O}_4$  electrodes are ~2005/1307  $\text{mAh g}^{-1}$  and ~1843/1296  $\text{mAh g}^{-1}$  with a Coulombic efficiency of ~65% and ~70%, respectively. The obtained initial capacity loss can be credited to the inevitable formation of the SEI layer owing to the electrolyte decomposition on the electrode surfaces.<sup>[33]</sup> However, both the electrodes in the successive cycles delivered high reversible discharge/charge capacities such as ~783/769  $\text{mAh g}^{-1}$  and ~1052/1035  $\text{mAh g}^{-1}$  for the 200<sup>th</sup> cycles, respectively with almost 100% Coulombic efficiency. More importantly, it can be also seen that the obtained capacity of the nanocomposite electrode in the 200<sup>th</sup> discharge-charge cycle is still higher than the theoretical capacity of  $\text{NiCo}_2\text{O}_4$  (890  $\text{mAh g}^{-1}$ ).

The differential capacity ( $dQ/dV$ ) curves for pure  $\text{NiCo}_2\text{O}_4$  and  $\text{NiCo}_2\text{O}_4/\text{Co}_3\text{O}_4$  nanocomposite electrodes are also investigated in the voltage range of 0.01–3.0 V as shown in Figure 7(c, d). Similar to galvanostatic charge/discharge results, the reduction peaks obtained at the voltages of ~1.01 V and ~1.10 V for both electrodes can be also seen at the 50<sup>th</sup> cycle due to the same reason as discussed above. After 50 cycles, the redox peak intensity of pure  $\text{NiCo}_2\text{O}_4$  electrode gradually decreases as the cycle number increases due to the deduction in the electrochemical activity of the material, i.e., poor  $\text{Li}^+$  ion kinetics and the deficiency of  $\text{Li}^+$  ion pathways.<sup>[34,35]</sup> However, the decrease in the redox peak intensity of  $\text{NiCo}_2\text{O}_4/\text{Co}_3\text{O}_4$  nanocomposite electrode is slow in comparison to pure, which is presumably due to the synergistic effect between two different metal oxides of  $\text{NiCo}_2\text{O}_4$  and  $\text{Co}_3\text{O}_4$ , resulting more active sites during the repeated charge/discharge cycles. In addition, it is also found that the differential capacity of the

$\text{NiCo}_2\text{O}_4/\text{Co}_3\text{O}_4$  electrode is higher than the pure  $\text{NiCo}_2\text{O}_4$  after 400<sup>th</sup> cycles, indicating the presence of an extra phase of  $\text{Co}_3\text{O}_4$  enhanced the  $\text{Li}^+$  storage activity.

Furthermore, the long-term cycling performance initially at 0.1 C for the first three cycles and then at 0.5 C for consecutive 500 cycles is investigated, as shown in Figure 8(a). The purpose to carry out the initial three cycles at the lower current rate of 0.1 C is to activate and stabilize the electrode material as well as to improve SEI formation.<sup>[36]</sup> It is worth mentioning that both the electrodes have first serious capacity decay until nearly 75 cycles and thereafter the capacity started increasing. It is believed that the obtained behavior is due to the formation of SEI film on the electrode surfaces, which restricts the  $\text{Li}^+$  ions extraction from the electrode to the electrolyte along with the mechanical deterioration owing to the volume changes.<sup>[37]</sup> Notably, the Coulombic efficiency of both the electrodes of pure  $\text{NiCo}_2\text{O}_4$  and  $\text{NiCo}_2\text{O}_4/\text{Co}_3\text{O}_4$  also shows a slight decrease in the same range of cycle numbers, certifying the capacity decay in the electrode materials. Thereafter, the charge capacity of both electrodes gradually started increasing in the further cycles, which can be ascribed to the activation process in the electrode materials as the SEI is also more effective in passivating the active materials. The following two facts can be considered to explain this phenomenon: i) it is obvious that the  $\text{Li}^+$  lithium ions inserted during discharge induced the volume expansion/contraction along with the formation of SEI layer, which further blocked to some extent the transfer of  $\text{Li}^+$  ions from electrolyte to electrode, resulting the conversion reaction may not be fully reversible and thereby the capacity loss during successive cycles. This factor may also be responsible for the low Coulombic efficiency in the first cycle. ii) However, after repeated cycles, the electrodes become stretchable and feasible to effectively permit the electrolyte to access the inner part of the active materials, and thus, the electrode|electrolyte contact area is enhanced (improved “wetting”), leading to the reversible conversion reaction followed by high specific capacity.<sup>[38,39]</sup> Similar behavior was also found in other reported ternary transition metal oxide anodes.<sup>[39–41]</sup> Over the prolonged cycling until ~400 cycles, the  $\text{NiCo}_2\text{O}_4/\text{Co}_3\text{O}_4$  nanocomposite electrode exhibits the highest charge capacity of ~1234  $\text{mAh g}^{-1}$  compared to pure  $\text{NiCo}_2\text{O}_4$  (~1126  $\text{mAh g}^{-1}$ ), which may be due to the strong synergistic effect between

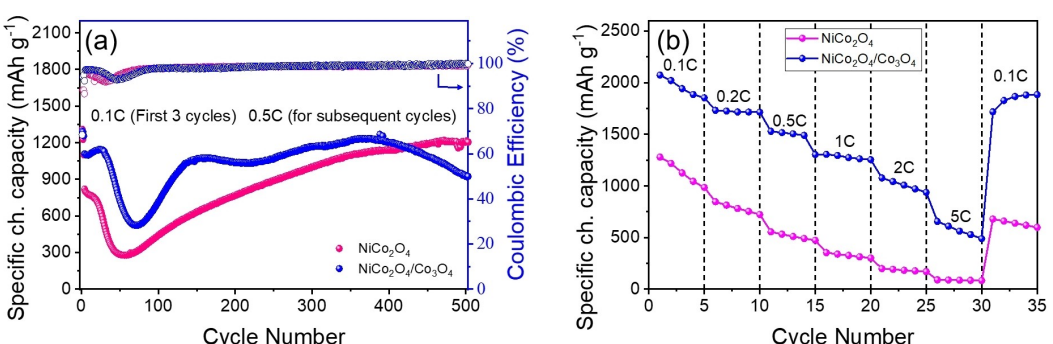


Figure 8. a) Cycle performance including coulombic efficiency up to 500 cycles; b) rate performances at various C-rates of pure  $\text{NiCo}_2\text{O}_4$  and  $\text{NiCo}_2\text{O}_4/\text{Co}_3\text{O}_4$  electrodes.

$\text{NiCo}_2\text{O}_4$  and  $\text{Co}_3\text{O}_4$ , resulting in efficient charge storage sites to enhance the redox reactions, numerous porous channels to offer short diffusion paths for  $\text{Li}^+$  ions, and sequentially buffer the volume changes obtained during cycling. However, later on, the nanocomposite electrode capacity after 400 cycles started falling down, while pure electrode capacity keeps increasing till 500 cycles. As stated above, though the nanocomposite electrode has high porosity than the pure electrode, it could not offer high stability to the current morphology during long-range cycling, resulting in the nanocomposite electrode getting pulverized after 500 cycles due to the repeated volume expansion/contraction.

Figure 8(b) shows the comparative rate capability of the pure  $\text{NiCo}_2\text{O}_4$  and  $\text{NiCo}_2\text{O}_4/\text{Co}_3\text{O}_4$  nanocomposite electrodes at various C-rates. It is obvious that the nanocomposite electrode has a higher charge capacity than the pure sample at different rates. Thus, the nanocomposite electrode delivers the charge (= de-lithiation) capacity of  $\sim 2073$ ,  $\sim 1731$ ,  $\sim 1528$ ,  $\sim 1305$ ,  $\sim 1077$  and  $\sim 656 \text{ mAh g}^{-1}$  at  $0.1 \text{ C}$ ,  $0.2 \text{ C}$ ,  $0.5 \text{ C}$ ,  $1 \text{ C}$ ,  $2 \text{ C}$  and  $5 \text{ C}$ , respectively. It can also be seen that when the current rate returned back to  $0.1 \text{ C}$  at 35 cycles, the nanocomposite electrode recovered nearly  $\sim 82\%$  ( $\sim 1717 \text{ mAh g}^{-1}$ ) of its initial capacity, which indicates better stability of the nanocomposite electrode. In contrast, pure  $\text{NiCo}_2\text{O}_4$  electrode delivered only  $\sim 1279$ ,  $\sim 847$ ,  $\sim 556$ ,  $\sim 354$ ,  $\sim 200$ , and  $\sim 91 \text{ mAh g}^{-1}$ , respectively at the same current rates. However, when the current rate

returned back to  $0.1 \text{ C}$ , the reversible capacity was only  $\sim 53\%$  ( $\sim 679 \text{ mAh g}^{-1}$ ), which is not very remarkable. Apart from the synergistic effects between the  $\text{NiCo}_2\text{O}_4$  and  $\text{Co}_3\text{O}_4$ , it is also believed that the extra phase of  $\text{Co}_3\text{O}_4$  imparts in the electrochemical reactions and exhibits high capacity due to the storage of  $8 \text{ Li}^+$  ions per formula unit ( $\text{Co}_3\text{O}_4 + 8\text{Li}^+ + 8\text{e}^- \rightarrow 3\text{Co} + 4\text{Li}_2\text{O}$ ). In addition, a comparative study of the electrochemical performances of the current work and the previously reported literature of  $\text{NiCo}_2\text{O}_4$  electrode materials based on different morphologies has been summarized in Table 2.<sup>[13,20,29,42–48]</sup> It can be concluded that the nanowire morphology of  $\text{NiCo}_2\text{O}_4/\text{Co}_3\text{O}_4$  electrode exhibits high reversible capacity and superior cycling stability than others.

In order to mainly evaluate the charge transfer resistance during the electrochemical reactions, electrochemical impedance spectroscopy (EIS) was performed on both the pure  $\text{NiCo}_2\text{O}_4$  and  $\text{NiCo}_2\text{O}_4/\text{Co}_3\text{O}_4$  nanocomposite electrodes after 1<sup>st</sup> and 500<sup>th</sup> cycles and the obtained results are displayed in Figure 9(a) and (b), respectively. The trend of EIS curves for both the electrodes are almost similar after 1<sup>st</sup> and 500<sup>th</sup> cycles. Both the electrode shows a semi-circle in the high-frequency region corresponds to the charge transfer resistance ( $R_{ct}$ ) related to the electrode/electrolyte interface and a slanted line in the low-frequency region belongs to the Warburg resistance ( $Z_w$ ) associated with the diffusion of  $\text{Li}^+$  ions within the electrode.<sup>[11,49]</sup> It can be noticed that the  $R_{ct}$  values of  $\text{NiCo}_2\text{O}_4/\text{Co}_3\text{O}_4$

**Table 2.** A comparative study between the electrochemical performances of the current work and various  $\text{NiCo}_2\text{O}_4$ -based electrode materials based on different morphologies.

Materials	Morphology	Synthesis method	Capacity/ current density/ cycle number	Ref.
$\text{NiCo}_2\text{O}_4/\text{TiO}_2$	Flower-like consisting of nanosheet	Hydrothermal	$\sim 1033 \text{ mAh g}^{-1}/100 \text{ mA g}^{-1}/100$	[29]
$\text{NiCo}_2\text{O}_4$	Dried-plum like	Spray pyrolysis	$801 \text{ mAh g}^{-1}/100 \text{ mA g}^{-1}/50$	[43]
$\text{NiCo}_2\text{O}_4$	double-hemispherical	Precipitation method	$585 \text{ mAh g}^{-1}/400 \text{ mA g}^{-1}/100$	[42]
$\text{NiCo}_2\text{O}_4$	Nanosheets	Microwave method	$767 \text{ mAh g}^{-1}/100 \text{ mA g}^{-1}/50$	[45]
$\text{NiO/NiCo}_2\text{O}_4$	Sphere-like	Pyrolysis	$920 \text{ mAh g}^{-1}/100 \text{ mA g}^{-1}/100$	[46]
$\text{NiCo}_2\text{O}_4$	Porous nanodisks	Hydrothermal method	$\sim 673 \text{ mAh g}^{-1}/0.5 \text{ C}/350$	[13]
rGO/ $\text{NiCo}_2\text{O}_4$	Nanosheets	Low-temperature solution method	$\sim 656 \text{ mAh g}^{-1}/500 \text{ mA g}^{-1}/50$	[47]
$\text{NiCo}_2\text{O}_4$	Microflowers	Solvothermal method	$212 \text{ mAh g}^{-1}/100 \text{ mA g}^{-1}/50$	[44]
PPC/ $\text{NiCo}_2\text{O}_4$	Both nanoneedles and nanoparticles	Hydrothermal method	$500 \text{ mAh g}^{-1}/50 \text{ mA g}^{-1}/120$	[20]
$\text{NiCo}_2\text{O}_4@\text{SnO}_2$ -HSs	Core-shell nanostructure	Hydrothermal method	$654 \text{ mAh g}^{-1}/100 \text{ mA g}^{-1}/100$	[48]
$\text{NiCo}_2\text{O}_4/\text{Co}_3\text{O}_4$	Nanowire	Hydrothermal method	$\sim 1234 \text{ mAh g}^{-1}/0.5 \text{ C}/400$	This work

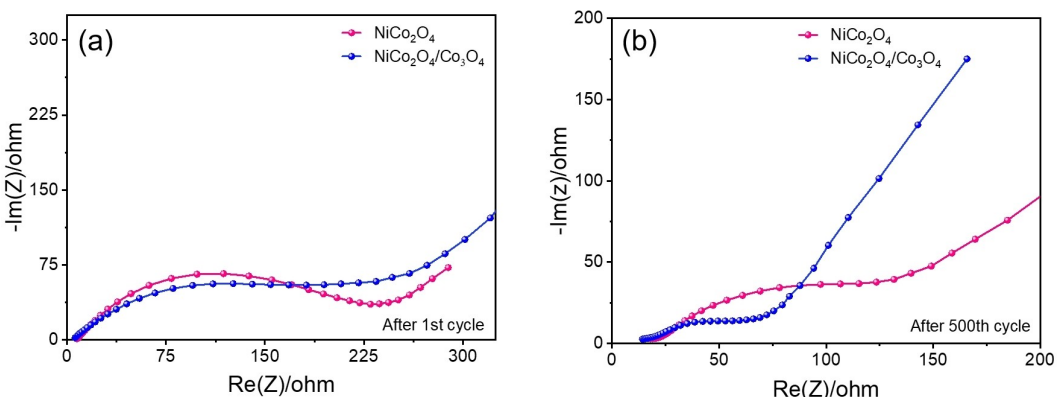


**Figure 9.** Nyquist plots of pure  $\text{NiCo}_2\text{O}_4$  and  $\text{NiCo}_2\text{O}_4/\text{Co}_3\text{O}_4$  electrodes a) after the 1<sup>st</sup> cycle and b) after the 500<sup>th</sup> cycle.

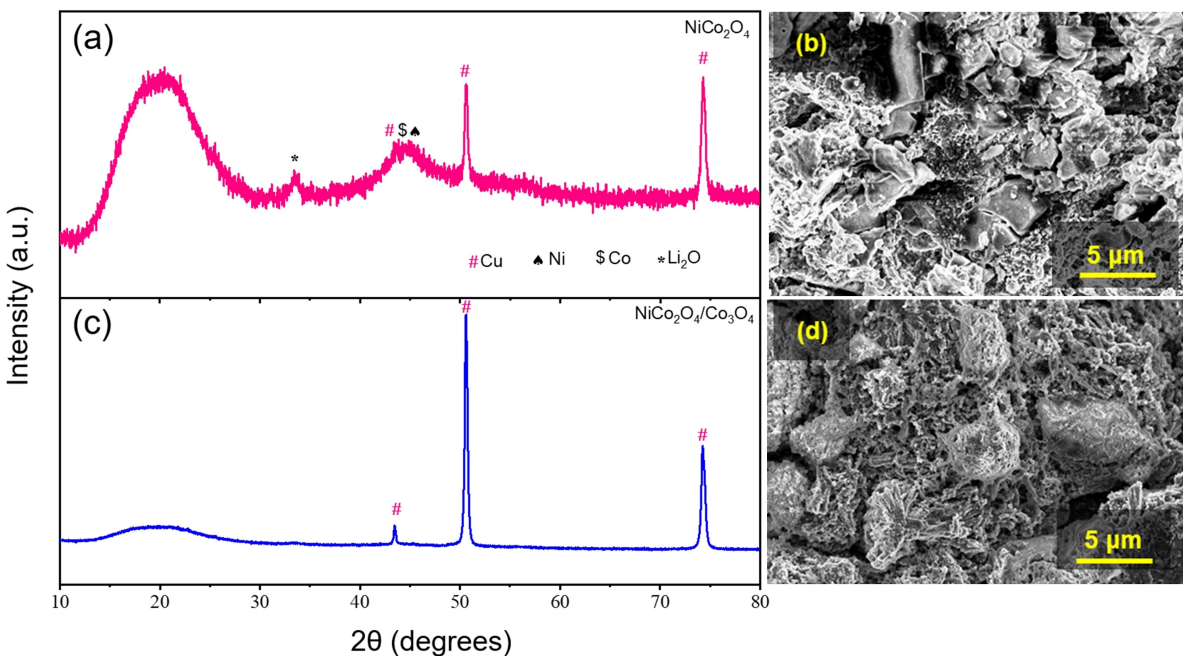


Figure 10. *ex-situ* XRD and SEM patterns of a, b) pure  $\text{NiCo}_2\text{O}_4$  and c, d)  $\text{NiCo}_2\text{O}_4/\text{Co}_3\text{O}_4$  electrodes after 500<sup>th</sup> cycles.

$\text{Co}_3\text{O}_4$  electrodes are found to be less in both the cases after the 1<sup>st</sup> and 500<sup>th</sup> cycle compared to the pure  $\text{NiCo}_2\text{O}_4$  electrode, which suggests that the synergistic effects with high porosity provide more active sites for fast charge transfer at the electrode|electrolyte interface with better reaction kinetics.<sup>[50]</sup> In addition, the  $\text{NiCo}_2\text{O}_4/\text{Co}_3\text{O}_4$  nanocomposite electrode shows steeper slopes in the low-frequency region (Warburg impedance), which is mainly due to the small diffusion barrier for  $\text{Li}^+$  ions compared to the pure  $\text{NiCo}_2\text{O}_4$  electrode.<sup>[49]</sup> It is also believed that the extra phase of  $\text{Co}_3\text{O}_4$  alleviates the structural change of  $\text{NiCo}_2\text{O}_4$  and lowers the impedance during the charge/discharge processes.

*Ex-situ* XRD analysis was also performed after 500 cycles to investigate the reversibility of the electrode materials of pure  $\text{NiCo}_2\text{O}_4$  and  $\text{NiCo}_2\text{O}_4/\text{Co}_3\text{O}_4$  nanocomposite, as displayed in Figure 10(a) and (c), respectively. The three intense reflections can be easily seen in the XRD patterns, which are copper current collector reflections. Furthermore, the reflections of  $\text{NiCo}_2\text{O}_4$  and  $\text{Co}_3\text{O}_4$  disappeared after 500 cycles in the nanocomposite sample, whereas the three reflections located at 2 theta values of 44.4, 44.2, and 33.6 were found for the pure  $\text{NiCo}_2\text{O}_4$  electrode, which can be ascribed to the Ni (JCPDS file no: 04–0850), Co (JCPDS file no: 15–0806) and  $\text{Li}_2\text{O}$  (JCPDS file no: 12–0254), respectively.<sup>[51]</sup> This clearly leads to the confirmation of the conversion reaction in pure  $\text{NiCo}_2\text{O}_4$  electrode even after 500 cycles, as shown in Equation (1). The existence of diffraction peaks of Ni, Co and  $\text{Li}_2\text{O}$  in Figure 10(a) implies that the electrode material of pure  $\text{NiCo}_2\text{O}_4$  is not fully deteriorated, whereas no such peaks are found in  $\text{NiCo}_2\text{O}_4/\text{Co}_3\text{O}_4$  nanocomposite electrode after 500 cycles. To further evaluate the morphological stability of the cycled electrodes of pure  $\text{NiCo}_2\text{O}_4$  and  $\text{NiCo}_2\text{O}_4/\text{Co}_3\text{O}_4$  nanocomposite, *ex-situ* SEM analysis was performed after 500 cycles and the obtained results are

displayed in Figure 10(b) and (d), respectively. As it is already found in FE-SEM (Figure 2) and FE-TEM (Figure 3) analysis that the nanocomposite sample is more highly porous than the pure, the same porous behavior can be also observed in the *ex-situ* morphology of the nanocomposite electrode. It is believed that the repeated  $\text{Li}^+$  insertion/de-insertion further enhanced the porosity in the cycled nanocomposite electrode, which clearly suggests the incompetency of this electrode to hold its morphology during long-range cycling. In contrast, Figure 10(b) shows the surface morphology of pure  $\text{NiCo}_2\text{O}_4$  electrode without porosity, which thereby indicates that the pure electrode has the potential to retain the structure and avoid the pulverization of electrode materials during cycling.

Based on the above results, it can be summarized that  $\text{Co}_3\text{O}_4$  played two different roles in the  $\text{NiCo}_2\text{O}_4/\text{Co}_3\text{O}_4$  nanocomposite sample: i)  $\text{Co}_3\text{O}_4$  as an active material provides massive active sites and enhanced the contacts between the electrodes and electrolyte, which significantly shorten the  $\text{Li}^+$  diffusion pathway for fast  $\text{Li}^+$  transport into the electrode and the synergistic effect between two different metal oxides improve the electrochemical performance of the material. ii) Meanwhile, the formation of an additional phase of  $\text{Co}_3\text{O}_4$  may also enhance the porosity of nanocomposite  $\text{NiCo}_2\text{O}_4/\text{Co}_3\text{O}_4$  material, which makes the morphology very fragile. Thereby, the instability of the nanocomposite structure causes the decay in capacity and restricts cycling stability.

## Conclusion

In summary, 1D nanowires of  $\text{NiCo}_2\text{O}_4/\text{Co}_3\text{O}_4$  nanocomposite were successfully synthesized without using any additional precursor of  $\text{Co}_3\text{O}_4$  from the exterior via one-step hydrothermal

method by simply controlling the molar ratio of Ni and Co followed by the calcination at 400 °C for 4 h in air atmosphere. Pure NiCo<sub>2</sub>O<sub>4</sub> was also synthesized under the same protocol using the stoichiometric ratio of Ni and Co for comparison. The structural analysis revealed that the nanowire-like morphology of each NiCo<sub>2</sub>O<sub>4</sub> and NiCo<sub>2</sub>O<sub>4</sub>/Co<sub>3</sub>O<sub>4</sub> nanocomposite is mainly composed of small, interconnected nanoparticles, which are in the range of ~9–20 nm. BET analysis confirmed the mesoporosity of the materials. In comparison, pure NiCo<sub>2</sub>O<sub>4</sub> material shows a high surface area (~56.2 m<sup>2</sup> g<sup>-1</sup>) than NiCo<sub>2</sub>O<sub>4</sub>/Co<sub>3</sub>O<sub>4</sub> nanocomposite (~47.1 m<sup>2</sup> g<sup>-1</sup>) with a pore diameter in the range of 7.5–15.5 nm and 9–24 nm, respectively. When evaluated as an anode material for LIB cells, the NiCo<sub>2</sub>O<sub>4</sub>/Co<sub>3</sub>O<sub>4</sub> electrode material shows excellent performance up to 400 cycles with a high lithium storage capacity of ~1234 mAh g<sup>-1</sup> at 0.5 C and a superior rate capability of ~1305 mAh g<sup>-1</sup> at 1 C, which can be ascribed to the synergistic effect between NiCo<sub>2</sub>O<sub>4</sub> and Co<sub>3</sub>O<sub>4</sub> with porous architecture, resulting high specific capacity due to the availability of more active sites to enhance the redox reactions and lower Li<sup>+</sup> diffusion pathway. Meanwhile, after 400<sup>th</sup> cycles, the nanocomposite capacity started decreasing as compared to the pure NiCo<sub>2</sub>O<sub>4</sub>, which could be credited to the high porosity of the nanostructure, consequentially showing degradation of the electrode material during long-range cycling.

## Experimental

### Material synthesis

The nanocomposite of NiCo<sub>2</sub>O<sub>4</sub>/Co<sub>3</sub>O<sub>4</sub> was prepared by facile hydrothermal synthesis method using nonstoichiometric ratio of Ni:Co as 2:6. In a typical synthesis, 2 mM of nickel (II) nitrate hexahydrate, (Ni(NO<sub>3</sub>)<sub>2</sub>·6H<sub>2</sub>O, Fischer Scientific, 98%, India), 6 mM of Cobalt (II) nitrate hexahydrate, (Co(NO<sub>3</sub>)<sub>2</sub>·6H<sub>2</sub>O, Fischer Scientific, 97%–101% India) and 0.3 g of urea were first dissolved in 40 mL of deionized (DI) water and 30 mL ethylene glycol (EG), with continuous stirring. Then, a calculated amount of polyvinyl pyrrolidone (PVP,  $M_w$ =40000 g/mol, Alfa Aesar, China) was also added to the above solution under stirring to make the solution homogeneous. Thereafter, it was transferred into a Teflon-lined stainless autoclave (100 mL) for hydrothermal treatment and placed at 150 °C for 14 h. After natural cooling, the resultant product was collected and centrifuged with DI water and ethanol for many times followed by drying in an oven at 60 °C for overnight. Then, the dried product was calcined at 400 °C for 4 h in an air atmosphere. For comparison, pure NiCo<sub>2</sub>O<sub>4</sub> was also prepared with a similar procedure using stoichiometric ratio of Ni:Co as 2:4.

### Material characterization

Thermal analysis was performed on a Shimadzu simultaneous DTA-TG system (DTG-60H) between room temp. to 700 °C in an air atmosphere with a heating rate of 10 °C min<sup>-1</sup>. The phase purity and the crystal structure of the calcined samples were identified by powder X-ray diffraction (XRD) using Shimadzu X-ray diffractometer with Cu K $\alpha$  radiation ( $\lambda$ =1.5406 Å). The surface morphology, particle size, and detailed microstructure analysis were characterized by field-emission scanning electron microscopy (FE-SEM Zeiss

Gemini SEM 500 Thermal field emission type, Zeiss) and transmission electron microscopy (FE-TEM, Technai 200, FEI). The chemical compositions of both samples were analyzed with an inductively coupled plasma-atomic emission spectrometer (ICP-AES) using an ARCOS, Simultaneous ICP Spectrometer. The surface area including pore size was carried out by adsorption/desorption isotherms using Brunauer-Emmett-Teller (*Micromeritics Instrument Corp. Gemini-V*).

### Electrode preparation

The calcined samples as active materials were uniformly mixed with carbon black (Super C65, *Imerys Graphite & Carbon*) as a conducting agent and polyvinylidene difluoride (PVDF; Solef 5130, *Solvay*) as a binder with the weight ratio of 60:20:20. For paste preparation, all the solid materials were dissolved in *N*-methyl-2-pyrrolidone (NMP; anhydrous, purity: 99.5%, *Sigma-Aldrich*) solvent in a planetary centrifugal mixer (20 min, 1700 rpm, ARM 310CE, *Thinky Corporation*). The electrode paste was coated onto a copper foil (20 µm, *Nippon foil*) with a doctor blade (*Zehntner GmbH*) and an automatic film applicator (*Sheen Instruments*). The electrode sheets were then dried for 2 h in an atmospheric oven at 80 °C and calendered (CLP 2025, *Hohsen Corp.*). The electrodes were then punched out with Ø=14 mm in diameter discs and dried in a Büchi B-585 glass drying oven under reduced pressure (<5 × 10<sup>-2</sup> bar) for 8 h at 90 °C. The average mass loading of the electrodes was ~0.25 mg cm<sup>-2</sup>.

### Cell assembly and electrochemical characterization

The 2032 coin-type cells (two-electrode configuration)<sup>[52]</sup> were assembled in a dry room with a dew point of at least -50 °C (relative humidity of 0.16%). Lithium metal was used as a negative electrode (Ø=15 mm, lithium metal foil, 500 µm in thickness; battery grade: purity ≥99.9%, *China Energy Lithium Co.*) and a polymer membrane (Ø=16 mm, Celgard 2500, *Celgard*) served as a separator. The electrolyte was 1 M LiPF<sub>6</sub> dissolved in a 1:1 (volume ratio) mixture of ethylene carbonate and dimethyl carbonate (battery grade; *Solvionic*). The electrochemical performance was evaluated on a MacCor series 4000 battery test system at room temperature within the voltage range of 0.01 and 3.0 V at different C-rates. Electrochemical impedance spectroscopy (EIS) were also performed using a VMP3 multi-channel potentiostat-galvanostat system (*Biologic Science Instruments*) to measure the change in charge transfer resistance of the electrodes before and after cycling. All the electrochemical studies were performed three times by parallel experiments to clarify reproducibility.

### Acknowledgements

A. T. would like to express her sincere gratitude to the CSIR, New Delhi, India for the award of senior research fellowship. She would also like to thank USIC for providing instrumentation facility. E. A. thanks the Ministry for Culture and Science of North-Rhine Westphalia (Germany) for funding this work within the International Graduate School for Battery Chemistry, Characterization, Analysis, Recycling and Application (BACCARA). In addition, we greatly acknowledge Andre Bar for graphics support. A.K.R. is grateful to University Grants Commission (UGC) for the position under UGC-FRP scheme (FRP ID: 57304). This work was mainly supported by the Faculty Research Programme Grant (Ref. No./

IoE/2021/12/FRP), sanctioned by Institution of Eminence, University of Delhi.

## Conflict of Interest

The authors declare no conflict of interest.

## Data Availability Statement

The data that support the findings of this study are available on request from the corresponding author. The data are not publicly available due to privacy or ethical restrictions.

**Keywords:** anode • lithium-ion battery • mesoporous • nanowire • NiCo<sub>2</sub>O<sub>4</sub>

- [1] J. Huo, G. Zhang, Y. Wang, *J. Chem. Technol. Biotechnol.* **2020**, *96*, 142–146.
- [2] R. Schmuck, R. Wagner, G. Hörpel, T. Placke, M. Winter, *Nat. Energy* **2018**, *3*, 267–278.
- [3] W. An, B. Gao, S. Mei, B. Xiang, J. Fu, L. Wang, Q. Zhang, P. K. Chu, K. Huo, *Nat. Commun.* **2019**, *10*, 1447–1458.
- [4] Q. Wang, L. Jiang, Y. Yu, J. Sun, *Nano Energy* **2019**, *55*, 93–114.
- [5] Y. Zhang, K. Hu, J. Ren, Y. Wu, N. Yu, A. Feng, Z. Huang, Z. Jia, G. Wu, *Dalton Trans.* **2019**, *48*, 17683–17690.
- [6] Y. Meng, Y. Liu, J. He, X. Sun, A. Palmieri, Y. Gu, X. Zheng, Y. Dang, W. Mustain, S. L. Suib, *ACS Appl. Energ. Mater.* **2021**, *4*, 5424–5433.
- [7] Y. Sun, F. Huang, S. Li, Y. Shen, A. Xie, *Nano Res.* **2017**, *10*, 3457–3467.
- [8] S. Mohapatra, S. V. Nair, D. Santhanagopalan, A. K. Rai, *Electrochim. Acta* **2016**, *206*, 217–225.
- [9] J. Singh, S. Lee, S. Kim, S. P. Singh, J. Kim, A. K. Rai, *J. Alloys Compd.* **2021**, *850*, 156755.
- [10] L. Zhang, J. Song, Y. Liu, X. Yuan, S. Guo, *J. Power Sources* **2018**, *379*, 68–73.
- [11] C. Zhang, Z. Xie, W. Yang, Y. Liang, D. Meng, X. He, P. Liang, Z. Zhang, *J. Power Sources* **2020**, *451*, 227761.
- [12] G. Xu, J. B. Sun, G. Y. Wang, X. F. Zhang, Z. P. Deng, L. H. Huo, S. Gao, *ACS Appl. Nano Mater.* **2021**, *4*, 6689–6699.
- [13] A. Jain, B. J. Paul, S. Kim, V. K. Jain, J. Kim, A. K. Rai, *J. Alloys Compd.* **2019**, *772*, 72–79.
- [14] L. Hou, X. Jiang, Y. Jiang, T. Jiao, R. Cui, S. Deng, J. Gao, Y. Guo, F. Gao, *ACS Omega* **2019**, *4*, 7565–7573.
- [15] L. Zhu, F. Li, T. Yao, T. Liu, J. Wang, Y. Li, H. Liu, R. Qian, Y. Liu, H. Wang, *Energy Fuels* **2020**, *34*, 11574–11580.
- [16] Y. Ren, X. Li, Y. Wang, Q. Gong, S. Gu, T. Gao, X. Sun, G. Zhou, *J. Mater. Sci. Technol.* **2022**, *102*, 186–194.
- [17] X. Y. Yu, X. W. Lou, *Adv. Energy Mater.* **2018**, *8*, 1701592.
- [18] I. T. Papadas, A. Ioakeimidis, G. S. Armatas, S. A. Choulis, *Adv. Sci.* **2018**, *5*, 1701029.
- [19] L. Li, Y. Ding, D. Yu, L. Li, S. Ramakrishna, S. Peng, *J. Alloys Compd.* **2019**, *777*, 1286–1293.
- [20] Z. Wang, Y. Xia, L. Liu, A. Wang, Y. Zhang, X. Liu, *Energy Fuels* **2020**, *34*, 13111–13117.
- [21] Q. Chu, B. Yang, W. Wang, W. Tong, X. Wang, X. Liu, J. Chen, *ChemistrySelect* **2016**, *1*, 5569–5573.
- [22] Y. Zhu, Y. Huang, M. Wang, K. Wang, M. Yu, X. Chen, Z. Zhang, *Ceram. Int.* **2018**, *44*, 21690–21698.
- [23] W. Chen, L. Wei, Z. Lin, Q. Liu, Y. Chen, Y. Lin, Z. Huang, *RSC Adv.* **2017**, *7*, 47602–47613.
- [24] Z. Zhang, Y. Huang, J. Yan, C. Li, X. Chen, Y. Zhu, *Appl. Surf. Sci.* **2019**, *473*, 266–274.
- [25] J. Xu, L. He, Y. Wang, C. Zhang, Y. Zhang, *Electrochim. Acta* **2016**, *191*, 417–425.
- [26] Y. Sun, X. Zuo, D. Xu, D. Sun, X. Zhang, S. Zeng, *ChemistrySelect* **2016**, *1*, 5129–5136.
- [27] M. Islam, G. Ali, M. G. Jeong, K. Y. Chung, K. W. Nam, H. G. Jung, *Int. J. Energy Res.* **2021**, *45*, 15036–15048.
- [28] D. Zhang, Y. Liu, L. Wu, L. Feng, W. Qin, *J. Solid State Chem.* **2021**, *295*, 121903.
- [29] X. Chu, C. Wang, L. Zhou, X. Yan, Y. Chi, X. Yang, *RSC Adv.* **2018**, *8*, 39879–39883.
- [30] B. Li, J. Feng, Y. Qian, S. Xiong, *J. Mater. Chem.* **2015**, *3*, 10336–10344.
- [31] Y. Li, X. Wu, S. Wang, W. Wang, Y. Xiang, C. Dai, Z. Liu, Z. He, X. Wu, *RSC Adv.* **2017**, *7*, 36909–36916.
- [32] Y. Li, X. Wu, *Ionics* **2018**, *24*, 1329–1337.
- [33] K. Chu, Z. Li, S. Xu, G. Yao, Y. Xu, P. Niu, F. Zheng, *Dalton Trans.* **2020**, *49*, 10808–10815.
- [34] A. Bothe, L. Gehrlein, Q. Fu, C. Li, J. Maibach, S. Dsoke, A. Balducci, *Batteries & Supercaps* **2022**, *5*, e202200152.
- [35] C. Ding, L. Wang, W. Zhou, D. Wang, Y. Du, G. Wen, *Chem. Eng. J.* **2018**, *353*, 340–349.
- [36] Y. Zhao, C. Liu, R. Yi, Z. Li, Y. Chen, Y. Li, I. Mitrovic, S. Taylor, P. Chalker, L. Yang, C. Zhao, *Electrochim. Acta* **2020**, *345*, 136203.
- [37] G. Xu, J. B. Sun, G. Y. Wang, X. F. Zhang, Z. P. Deng, L. H. Huo, S. Gao, *ACS Appl. Nano Mater.* **2021**, *4*, 6689–6699.
- [38] F. Fu, J. Li, Y. Yao, X. Qin, Y. Dou, H. Wang, J. Tsui, K. Y. Chan, M. Shao, *ACS Appl. Mater. Interfaces* **2017**, *9*, 16194–16201.
- [39] L. Zhu, F. Li, T. Yao, T. Liu, J. Wang, Y. Li, H. Lu, R. Qian, Y. Liu, H. Wang, *Energy Fuels* **2020**, *34*, 11574–11580.
- [40] X. Hou, S. Bai, S. Xue, X. Shang, Y. Fu, D. He, *J. Alloys Compd.* **2017**, *711*, 592–597.
- [41] Y. He, L. Xu, Y. Zhai, A. Li, X. Chen, *Chem. Commun.* **2015**, *51*, 14768–14771.
- [42] Y. Yang, G. Y. Huang, H. Sun, M. Ahmad, Q. Mou, H. Zhang, *J. Colloid Interface Sci.* **2018**, *529*, 357–365.
- [43] T. Li, X. Li, Z. Wang, H. Guo, Y. Li, *J. Mater. Chem. A* **2015**, *3*, 11970–11975.
- [44] J. Xu, L. He, W. Xu, H. Tang, H. Liu, T. Han, C. Zhang, Y. Zhang, *Electrochim. Acta* **2014**, *145*, 185–192.
- [45] A. K. Mondal, D. Su, S. Chen, K. Kretschmer, X. Xie, H. J. Ahn, G. Wang, *ChemPhysChem* **2015**, *16*, 169–175.
- [46] J. Chen, J. Jiang, S. Liu, J. Ren, Y. Lou, *Ionics* **2019**, *25*, 5787–5797.
- [47] G. Gao, H. B. Wu, X. W. Lou, *Adv. Energy Mater.* **2014**, *4*, 1400422.
- [48] G. Gao, H. B. Wu, S. Ding, X. W. Lou, *Small* **2015**, *11*, 432–436.
- [49] Y. Kang, Y. H. Zhang, Q. Shi, H. Shi, D. Xue, F. N. Shi, *J. Colloid Interface Sci.* **2021**, *585*, 705–715.
- [50] Z. Wu, H. Ye, B. Zhang, J. Song, Y. Wang, D. Yao, C. Wang, X. Xia, W. Lei, Q. Hao, *Langmuir* **2021**, *37*, 8426–8434.
- [51] F. Wang, Y. Liu, H. Wei, G. Wang, F. Ren, X. Liu, M. Chen, A. A. Volinsky, S. Wei, Y. B. He, *J. Alloys Compd.* **2020**, *839*, 155614.
- [52] R. Nölle, K. Beltrop, F. Holtstiege, J. Kasnatscheew, T. Placke, M. Winter, *Mater. Today* **2020**, *32*, 131–146.

Manuscript received: October 24, 2022

Revised manuscript received: December 19, 2022

Accepted manuscript online: December 27, 2022

Version of record online: January 5, 2023